Nano Research

Open Access

Research Article

Data-driven discovery of high-performance zinc-ion battery cathodes by a machine learning strategy integrating energy gradient and activation area ratio

Yating Deng[1,§], Yujie Jiang[1,§], Wei Li[1,§], Wanyi Li[1], Ruiyang Liang[2]✉, Bin Xiao[3], Vitaly Bondarenko[4], Hanna Bandarenka[4], Jinzhao Wang[1], Guohua Cai[1], Xiaoke Wang[1], Ting Li[1], Jing Zhang[1], Dehong Chen[1], Zhenjiang Li[1]✉, Xiuquan Gu[3], Yanwei Sui[3], Eugene Chubenko[4], and Jian Zhao[1]✉

[1] *College of Materials Science and Engineering, College of Chemistry and Molecular Engineering, State Key Laboratory of Advanced Optical Polymer and Manufacturing Technology, Qingdao University of Science and Technology, Qingdao 266042, China*
[2] *School of Materials Science and Engineering, Liaoning University of Technology, Jinzhou 121000, China*
[3] *School of Materials Science and Physics, China University of Mining and Technology, Xuzhou 221116, China*
[4] *Vitaly Bondarenko, Hanna Bandarenka, Eugene Chubenko, Belarusian State University of Informatics and Radioelectronics, 220013P, Brovka str. 6, Minsk, Belarus*
§ *Yating Deng, Yujie Jiang, and Wei Li contributed equally to this work.*

Cite this article: *Nano Research*, **2026**, *19*, 94908928. https://doi.org/10.26599/NR.2026.94908928

ABSTRACT: The heteroatom doping is considered a promising strategy for enhancing the performance of the MnO_2-based electrode materials for zinc-ion battery (ZIB). However, quickly discovering the high-performance doped-MnO_2 remains significant challenge to simultaneously give consideration to both the various metal types, doping concentration, and the essential screening mechanism. Herein, a novel research paradigm is developed by combining machine learning predictions with systematic experiments and theoretical calculations for solving this issue. The results simulated by machine learning from the two-dimensional perspective reveal that only when Co species are introduced into δ-MnO_2 can zinc ions (Zn^{2+}) maintain the smaller binding energy gradient distribution and larger activation area ratio among the constructed various doping system database, further achieving qualitative "structure–activity" descriptor. Moreover, the density functional theory (DFT) calculations systematically unveil optimal adsorption energy/Gibbs free energy, higher negative integral crystal orbital Hamilton population (−ICOHP) (0.0125 Ha), and lower Zn^{2+} diffusion barrier (0.978 eV) for moderate Co-doped δ-MnO_2 with oxygen vacancy ($Co_{(M)}$-δ-MnO_{2-x}, where (M) denotes moderate Co-doping concentration) compared with the other samples, which can preserve the Zn^{2+} adsorption/desorption equilibrium and the structure integration, and accelerate the reaction kinetics. Benefiting from these advantages, the obtained ZIB using the optimized cathode can present the large specific capacity of 655.7 mAh·g^{-1} at 0.5 A·g^{-1} and high rate capability (209.8 mAh·g^{-1} at 20 A·g^{-1}), which is far higher than those of the other compound cathode materials. This study offers new insights for the design and optimization of doped-δ-MnO_2 cathodes in ZIBs, and the obtained universal theoretical guidance is also suitable for constructing other high-performance layered electrode materials.

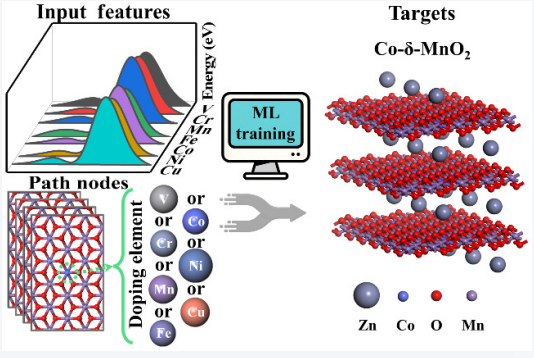

KEYWORDS: heteroatom doping, machine learning predictions, large specific capacity, high rate capability, reaction mechanism

Received: May 22, 2026; **Revised:** June 4, 2026
Accepted: June 9, 2026

✉Address correspondence to Ruiyang Liang, lry9319@lnut.edu.cn; Zhenjiang Li, zhenjiangli@qust.edu.cn; Jian Zhao, zjcc2016@qust.edu.cn

1 Introduction

Aqueous zinc-ion batteries (ZIBs) have been put into the spotlight in the field of sustainable energy storage by virtue of their nontoxic aqueous electrolyte and favorable ionic conductivity, as well as abundant and cheap zinc metal, large theoretical capacity of 820 mAh·g^{-1}, and low redox potential of Zn/Zn^{2+} (−0.76 V vs.

standard hydrogen electrode) [1, 2]. The cathodes of ZIBs commonly offer zinc storage active sites and definitively ascertain the energy/power density and cycle life of the battery, which are the significant factors restricting the large-scale applications of ZIBs at this stage [3]. In any case, developing large capacity, high rate, and durability cathode materials for ZIBs is an everlasting issue that must be solved. Currently, a series of cathode materials has been explored, such as manganese-based oxide, vanadium-based oxide, Prussian blue analogs, and layered sulfides. [4]. Among these candidates, δ-MnO_2 (birnessite MnO_2) is in vogue as satisfied species for ZIBs owing to low cost, environment-friendly, high theoretical capacity, and suitable operation voltage (~ 1.35 V) [5, 6]. Especially, its distinctive layer-by-layer architecture with ample interlayer spacing (~ 7.0 Å), which is conducive to rapid electron/ion transmission [5]. However, challenges like fast capacity degradation, sluggish reaction kinetics resulting from inferior intrinsic conductivity, and structure collapse after repeated Zn^{2+} insertion/extraction still remain in the cathodes [7]. Besides, Zn^{2+} with the large atomic mass and the high charge density can generally induce the electrostatic interaction with the host material, which enormously slows down the ion diffusion, resulting in undesirable rate performance [8]. Thus, there is a great need to conduct optimal design and structural regulation in δ-MnO_2 for settling these bottlenecks.

Recently, various routes have been proposed, including defect inducement, doping engineering, and pre-intercalating. [9–11]. In particular, heterogeneous metal atom doping has been deemed an effective way for modulating the electronic features, composition, and geometrical structure of the oxides, bringing about certain enhancements in ZIBs performance. To date, some significant progress has been made in the regulation of MnO_2 via such a doping technique, but how to precisely and quickly determine the suitable doped atom types and optimal concentration, further obtaining universal screening rules, has not been investigated. In addition, due to the intricate intrinsic features of the doped oxides, their capacity and rate capability are usually ascertained by diverse factors, such as equilibrium degree of ion adsorption/desorption, electron transport rate, ion diffusion barrier, and structure integration [12]. Thus, the complicated interdependence expresses tremendous troubles to rationally optimize the performances of MnO_2 and thereby widen its practical applications in ZIBs. Although there is currently a subconscious cognition that the encouraging doped oxides can be achieved through experimental preparation and a series of characterizations and tests, this method calls for constant trial and error, consuming substantial resources and time [13]. Under the circumstances, once the certain parameter or component is changed, a new iterative experiment loop is needed. This puzzle motivates insights into detailed structural characteristics of the doped oxides for expediting the development of high-performance doped MnO_2 beyond conventional trial-and-error routes [14].

Theoretical simulation techniques, such as density functional theory (DFT), molecular dynamics (MD), and Monte Carlo, have been extensively adopted to assist in probing the interactions between performances and complex microstructures of the doped materials without the need for experimentation [15, 16]. Regretfully, the models for various doping systems all need to be built, and any changes in components similarly give rise to a new round of parameter adjustments, further necessitating extra simulations. Also, it is difficult for the conventional simulation approach to hold the nonlinear and unpredictable correlations between structural parameters and properties of the doped materials [17]. Accordingly, the traditional approach to material discovery and refinement can consume a significant amount of computational resources and time. This is where data-driven machine learning (ML) strategy comes into play. As one of the typical representatives of artificial intelligence (AI) techniques, by virtue of high computational abilities and massive storage resources, ML provides a powerful methodology for unlocking the intricate mapping links between input structural characteristics and output property responses since ML can endow computers with the skill to extract patterns from data and automatically make predictions or decisions, all without performing further manual programming [18]. In previous studies, Wang et al. [19], Liow et al. [20], Cai et al. [21], etc. employed machine learning to investigate the correlation between structural parameters, elemental characteristics, synthesis conditions of different electrode systems, and their discharge capacity, Coulombic efficiency, or kinetics. Although the above works superficially uncovered positive or negative correlations between them, these efforts fall short of offering an in-depth investigation of the underlying mechanisms describing the performance-oriented design rules for the movement from empirical trial-and-error to data-driven material discovery. More importantly, the qualitatively complicated structure–activity relationships derived from two-dimensional (2D) perspective, which are exceedingly valuable for guiding the inverse design of the satisfied materials, have also not been explored. Therefore, the existing protruding bottleneck issues undoubtedly increase the difficulty in identifying the most suitable doping behavior, further tremendously impeding their applications in high-end energy storage systems.

Herein, we firstly used data-driven ML coupled with DFT calculations to realize a unique qualitative "structure–function" correlation between δ-MnO_2 structure variation and Zn^{2+} storage performances, which effectively determines the combination of suitable doping element and doping concentration, further quickly discovering the optimal ZIBs electrode materials ($Co_{(M)}$-δ-MnO_{2-x}, where (M) denotes moderate Co-doping concentration) among the constructed database. Moreover, the corresponding underlying mechanism is also systematically analyzed by simulating binding energy gradient distribution and activation area ratio at different current densities. DFT calculations validate that the preferred $Co_{(M)}$-δ-MnO_{2-x} owns prominent Zn^{2+} adsorption/desorption equilibrium, robust structure integration, and rapid reaction kinetics resulting from its optimal adsorption energy/Gibbs free energy, higher negative integral crystal orbital Hamilton population (–ICOHP), and lower Zn^{2+} diffusion barrier. Guided by this identified criterion, the advanced ZIB with the $Co_{(M)}$-δ-MnO_{2-x} cathode is successfully developed, which simultaneously achieves high capacity, superior rate capability, and long cycle stability. This study not only endows valuable insights into the quick discovery of high-performance doped-δ-MnO_2 ZIBs cathode materials through ML technique and DFT calculations, signifying a major step forward in the development of ZIBs, but also provides a universal design rule for screening exceptional layered electrode materials for other energy storage devices.

2 Results and discussion

ML technique and DFT calculations were utilized to predict the

qualitative "structure–function" descriptor between δ-MnO_2 doped with V, Cr, Fe, Co, Ni, Cu, and their capacity through simulating Zn^{2+} binding energy on the surface of the above electrode materials. Generally, the Zn^{2+} binding energy at various migration sites is often considered a key factor to determine their electrochemical performances. The crystal structure models of pure δ-MnO_2 (Fig. S1 in the Electronic Supplementary Material (ESM)) and different doping configurations are constructed using Materials Studio, and several representative Zn^{2+} adsorption and migration sites on the surface of each system are also selected (Figs. S2–S16 in the ESM). According to these models, the Zn^{2+} migration energy barriers on a certain one-dimensional diffusion path of pure δ-MnO_2 and δ-MnO_2 doped with V, Cr, Fe, Co, Ni, and Cu are calculated by traditional DFT calculations as presented in Fig. S2 in the ESM, which can provide the guidance to infer the optimal doped element in principle. However, the migration energy barriers are similar to some doping configurations, such as Co-doped δ-MnO_2 and Cu-doped δ-MnO_2, making it difficult to distinguish their performance advantages. Thus, to accurately establish the unique qualitative descriptor, the powerful ML strategy, combined with DFT calculations, is employed to systematically investigate the electrochemical performances of δ-MnO_2 and doped δ-MnO_2 as the ZIB cathodes. The core idea is to simulate Zn^{2+} binding energy from the two-dimensional material surface perspective, further predicting their capacity change tendency through two micro-quantitative indicators (binding energy gradient and activation area ratio). The binding energy gradient and the activation area ratio were calculated by Eqs. (S10) and (S11) in the ESM. The detailed schematic illustration of the workflow for machine learning prediction and screening is presented in Fig. 1(a). Clearly, the optimal cathode material Co-δ-MnO_2 can be identified through machine learning training, analysis, calculation, and screening procedures. Notably, the aforementioned calculated the Zn^{2+} binding energy at these sites, which are served as target variables for the subsequent ML models. Meanwhile, to construct the detailed input features of ML models, key atomic configuration parameters and intrinsic chemical bond information (Fig. S17 in the ESM), as well as abundant electronic structure data, including projected density of states (pDOS, Figs. S18–S24 in the ESM), crystal orbital Hamilton populations (COHP, Figs. S25–S31 in the ESM), crystal orbital overlap populations (COOP, Figs. S32–S38 in the ESM), integral COOP (ICOOP, Fig. S39(a) in the ESM), the center values of the elemental pDOS (Fig. S39(b) in the ESM), ICOHP (Fig. S39(c) in the ESM), corresponding bond lengths (Fig. S40 in the ESM) are also calculated and extracted, which collectively forms the raw feature datasets. During data preprocessing and feature engineering, the raw data underwent cleaning and was divided into training and testing sets in an 8:2 ratio. To enhance model efficiency and accuracy, initial features were screened based on the common knowledge of materials science. Also, the dimensionality reduction technique, such as principal component analysis (PCA) (Figs. S41–S43 in the ESM), was applied to extract crucial information, effectively reducing data dimensions and minimizing redundancy, thereby establishing a high-quality foundation for subsequent model training. Moreover, in the machine learning model construction and evaluation phase, multiple regression models, including linear regression, support vector regression, random forest (RF), and gradient boosting machines, were trained using the processed data. The coefficient of determination (R^2, Fig. 1(b)) is used to evaluate the predictive performance of 16 machine learning models, and three optimal machine learning models (RF, extra trees (ET), and extreme gradient boosting (XGB)) are selected based on their higher R^2 value. Moreover, through comprehensively comparing the actual versus predicted values plots of 16 models (Fig. 1(c) and Figs. S44–S49 in the ESM) in training and validation sets, the performance prediction error of the three optimal machine learning models is also relatively smaller than those of other models. Besides, their mean squared error (MSE, Fig. 1(d)), mean absolute error (MAE, Fig. S50 in the ESM), and K-fold (where K is the number of folds, set to 5 in this study) cross-validation (Fig. S51 in the ESM) are further analyzed, which determines that RF, ET, and XGB are really the optimal machine learning models, effectively guaranteeing the reliability for future data predictions. Then, the optimal machine learning models are employed to predict the Zn^{2+} binding energies at various two-dimensional surface sites of δ-MnO_2 and doped δ-MnO_2 cathode materials, and the corresponding results (binding energy distribution patterns) are presented in Fig. S52 in the ESM and Fig. 1(e), which enables the analysis of the capacity change tendency for the above various cathodes. Specifically, when the current density is smaller (e.g., 1–3 $A{\cdot}g^{-1}$), the charging and discharging process approaches thermodynamic equilibrium states with lower overpotential, in which the electrochemical performance is predominantly governed by intrinsic thermodynamic properties [22]. During the discharging stage, the activation sites binding energy is 0–1 eV; on the contrary, the activation sites binding energy is −1–0 eV (Fig. S53(a) in the ESM) at the charging state, which makes it hold a narrow energy window of −1–1 eV. Thus, we can clearly see from Fig. 1(e) that Co-doped δ-MnO_2 possesses higher proportion of stable adsorption sites within the optimal thermodynamic energy window, leading to the lower binding energy gradient and larger activation area ratio in comparison to other cathode materials, further achieving the highest capacity. Subsequently, according to the same analysis method as described above, the capacity of other cathodes is also evaluated, and the capacity ranking of these samples is as follows: M-doped δ-MnO_2 (M stands for the doped atom, Co > Cu > Ni > V > Cr > F). On the other hand, when the current density is increased to a higher level (e.g., 5–10 $A{\cdot}g^{-1}$), the rapid charge–discharge processes enforce the system into non-equilibrium states, where the high overpotential renders the kinetic limitation as the dominant bottleneck [22]. At this time, the corresponding energy window can also be expanded to −1.5–1.5 eV, which results in the higher binding energy gradients (Fig. 1(e) and Fig. S53(b) in the ESM). Under the circumstances, the high current density promotes rapid Zn^{2+} intercalation/extraction from the cathode materials in theory during the charging and discharging process, nevertheless, the higher binding energy gradients can restrict the Zn^{2+} movement, further constraining the activation area ratio. Therefore, based on the above analysis principles, from Fig. 1(e), the capacity of these samples derived from the high current density is arranged: M-doped δ-MnO_2 (Co > Ni ≈ Cu > Cr > Fe > V). Compared with the states at the low current density, the performance of Ni-, Cr-, and Fe-doped systems is relatively improved, resulting from more activation sites within the wider energy window, exhibiting superior kinetic responses during high current density cycling. However, in terms of V-doped δ-MnO_2, its structural features are difficult to adapt to rapid ion transport since the energy islands are generated because of the excessive binding energy gradients, giving rise to inferior capacity. In addition, to comprehensively evaluate the effectiveness of the

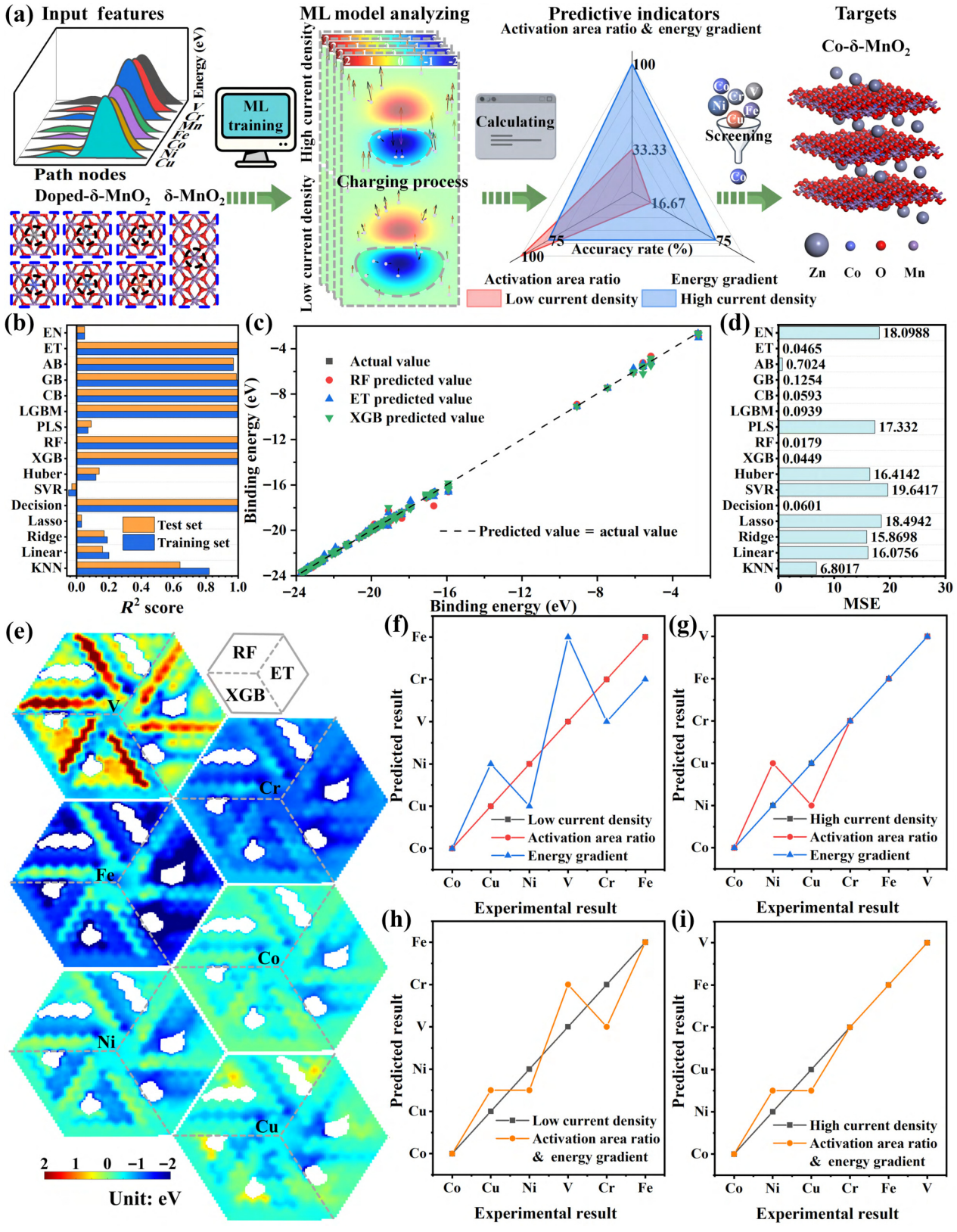

Figure 1 Machine learning combined with DFT calculations for predicting qualitative "structure–function" descriptor between δ-MnO_2 structure variation and Zn^{2+} storage performances through simulating Zn^{2+} binding energy on the surface of δ-MnO_2 doped with V, Cr, Fe, Co, Ni, Cu, and δ-MnO_2. (a) Schematic illustration of the workflow for machine learning prediction and screening. (b) R^2 values for the training and testing datasets corresponding to 16 machine learning models. (c) Actual versus predicted values of three optimal machine learning models. (d) MSE of 16 machine learning models. (e) Machine learning prediction results of the Zn^{2+} binding energy on the surface of doped δ-MnO_2 and δ-MnO_2. Comparisons of predicted results for the doped δ-MnO_2 with experimental data using single and dual indicators at low ((f) and (h)) and high ((g) and (i)) current densities.

single indicator (binding energy gradients or activation area ratio) and the dual-indicators synergistic prediction for the capacity of doped δ-MnO_2, the systematic comparative analyses were carried out among the predicted results caused by the single indicator and the dual-indicators, as well as the experimentally measured capacity shown in Figs. 1(f)–1(i). At the low current density, the predicted capacity of the doped δ-MnO_2 based on the activation area ratio is well consistent with the experimental results (Fig. S54 in the ESM). However, only when the binding energy gradient is considered, or both of the two indicators are taken into account simultaneously, the predicted result is really deviated from what is expected since Zn^{2+} ions migrate slowly at this state and possess sufficient time to bypass the high-binding-energy regions, thus the influence of the binding energy gradient can be ignored (Figs. 1(f) and 1(h)). Under the high current density circumstances, the predicted data resulted from any single indicator exhibits obvious errors. In contrast, the dual-indicators synergistic prediction strategy can effectively overcome the aforementioned limitations and realize the accurate capacity prediction, as shown in Figs. 1(g) and 1(i), which is in good agreement with the experimental results (Fig. S54 in the ESM). It is mainly attributed to the fact that the Zn^{2+} migration is enormously accelerated at high current density, which may cause the partial Zn^{2+} to move into the inactive high-binding-energy regions caused by the binding energy gradient. Therefore, the effect of binding energy gradient becomes more significant, so both of the dual-indicators need to be taken into consideration under such the conditions. The dual-indicators prediction strategy, especially at high current density, plays an important role in concluding the capacity of cathodes. To sum up, through analyzing the two indicators, the capacity change tendency of these cathode materials was predicted, further achieving the qualitative descriptor of their structure–activity relationship, and screening the optimal doping configuration. In order to further confirm the prediction results, we synthesized a series of metal atoms-doped δ-MnO_2 cathode materials, and the corresponding characterization, performance testing, and detailed mechanism analysis were also conducted as presented in Figs. 2–5.

A series of metal atoms with various concentrations (M = V, Cr, Fe, Co, Ni, and Cu)-doped δ-MnO_2 products were synthesized, and their electrochemical performances were also tested as shown in Fig. S54 in the ESM. The corresponding results clearly exhibit that the Co-doped δ-MnO_2 holds superior performance to those of other samples, which is well consistent with the machine learning prediction. Furthermore, for the sake of understanding the microscopic morphology and structural information of the pure δ-MnO_2 and δ-MnO_2 with low/moderate/high Co doping concentration (oxygen vacancies (OVs) are automatically introduced into the products, thus they can be marked as $Co_{(L)}$-δ-MnO_{2-x}, $Co_{(M)}$-δ-MnO_{2-x}, $Co_{(H)}$-δ-MnO_{2-x}, respectively, and the $Co_{(M)}$-δ-MnO_{2-x} owns highest specific capacity and rate performance among them demonstrated by the following discussion), the scanning electron microscopy (SEM) and transmission electron microscopy (TEM) were used to analyze these samples (Fig. 2 and Figs. S55(a)–S55(g) in the ESM). Obviously, the prepared pure δ-MnO_2 shows the homogeneous flower-like nanosphere morphology assembled by many nanosheets. After Co doping manipulation, these doped δ-MnO_2 products present almost the same morphological characteristics as the initial δ-MnO_2, as exhibited in Figs. S55(a)–S55(d) in the ESM, which confirms that the heteroatom doping produces a negligible effect on the morphology of δ-MnO_2. TEM images also explicitly verify the flower-like nanosphere structure of $Co_{(M)}$-δ-MnO_{2-x} composed of nanosheet arrays, and these nanosheets are intersected with each other, generating numerous free spaces (Figs. S55(e)–S55(g) in the ESM), which is in good agreement with the above SEM images. The distinct structure can offer sufficiently efficient active sites for redox reactions, endowing the $Co_{(M)}$-δ-MnO_{2-x} as an optimal cathode material. The high-resolution TEM (HRTEM) image (Fig. 2(a)) illustrates that the labeled lattice fringes with an interlayer spacing of 0.232 and 0.253 nm are attributed to the (003) and (200) planes of δ-MnO_2, respectively. The selected area electron diffraction (SAED) pattern reveals the diffraction rings corresponding to the (002), (200), $(\bar{1}11)$, and (203) planes, manifesting good crystallinity for the $Co_{(M)}$-δ-MnO_{2-x} (Fig. 2(b)). The energy dispersive X-ray spectroscopy (EDS) mapping indicates that O, Mn, and Co elements are uniformly distributed around the surface of the entire $Co_{(M)}$-δ-MnO_{2-x} nanosphere (Fig. 2(c)). The electron energy loss spectrum (EELS) is applied to achieve the atomic scale testimony of Mn and Co distribution (Fig. 2(d)). Obviously, the Mn and Co atomic information (641.8 and 653.0 eV; 780.6 and 795.9 eV, respectively) can be directly observed, further demonstrating the existence of Co species in MnO_2 lattice. In addition, the aberration-corrected high-angle annular dark-field scanning TEM (HAADF-STEM) image expresses the presentation of the atomically distributed Mn and Co species in the $Co_{(M)}$-δ-MnO_{2-x} lattice and demonstrates the representative [MnO_6] octahedral structure (Fig. 2(e)). From the HAADF-STEM image (Fig. 2(e)) and the corresponding intensity patterns of the marked e1 and e2 area (Fig. 2(g)), the position of Mn columns is revealed by the bright-dot contrast (high intensity), while the dark-dot contrast (low intensity) corresponds to Co heteroatoms. To achieve insights into the specific oxygen vacancy, high-resolution STEM annular bright-field (ABF) technique is conducted for determining the defects, as depicted in Fig. 2(f). The dispersion of the filled and empty apical oxygen sites is distinctly visible through ABF imaging. The red dashed circles in Fig. 2(f) indicate the positions of oxygen vacancies. The corresponding ABF intensity profiles (with inverse intensities) extracted from various regions labeled by f1 and f2 in Fig. 2(f) are displayed in Fig. 2(g), which reveals that the absence of image contrast at oxygen sites visually verifies the existence of oxygen vacancies.

X-ray diffraction (XRD) analysis is performed to determine the crystalline phases of the δ-MnO_2, $Co_{(L)}$-δ-MnO_{2-x}, $Co_{(M)}$-δ-MnO_{2-x} and $Co_{(H)}$-δ-MnO_{2-x} (Figs. S55(h) and S55(i) in the ESM). It can be seen from Fig. S55(h) in the ESM that all the diffraction peaks correspond to the standard PDF No. 80-1098 of layered birnessite-type δ-MnO_2. The absence of significant impurity peaks confirms the high phase purity of the synthesized materials. The enlarged diffraction peaks of (001), (002), and $(\bar{1}11)$ planes demonstrate that with the augmentation of Co atoms, these peaks position gradually shift to the lower angles, which reveals an expansion of the crystal lattice resulting from the Co doping (Fig. S55(h) in the ESM). X-ray photoelectron spectroscopy (XPS) is employed to analyze the chemical composition and elemental valence of δ-MnO_2, $Co_{(L)}$-δ-MnO_{2-x}, $Co_{(M)}$-δ-MnO_{2-x}, and $Co_{(H)}$-δ-MnO_{2-x}. The survey XPS spectra demonstrate the existence of Mn, O, and Co element signatures, confirming the successful introduction of Co heteroatom, as depicted in Fig. S55(j) in the ESM. The Mn 2p spectra of these samples are displayed in Fig. 2(h), and the peaks at 653.8 and 642.5 eV exist in the products, corresponding to $2p_{1/2}$ and

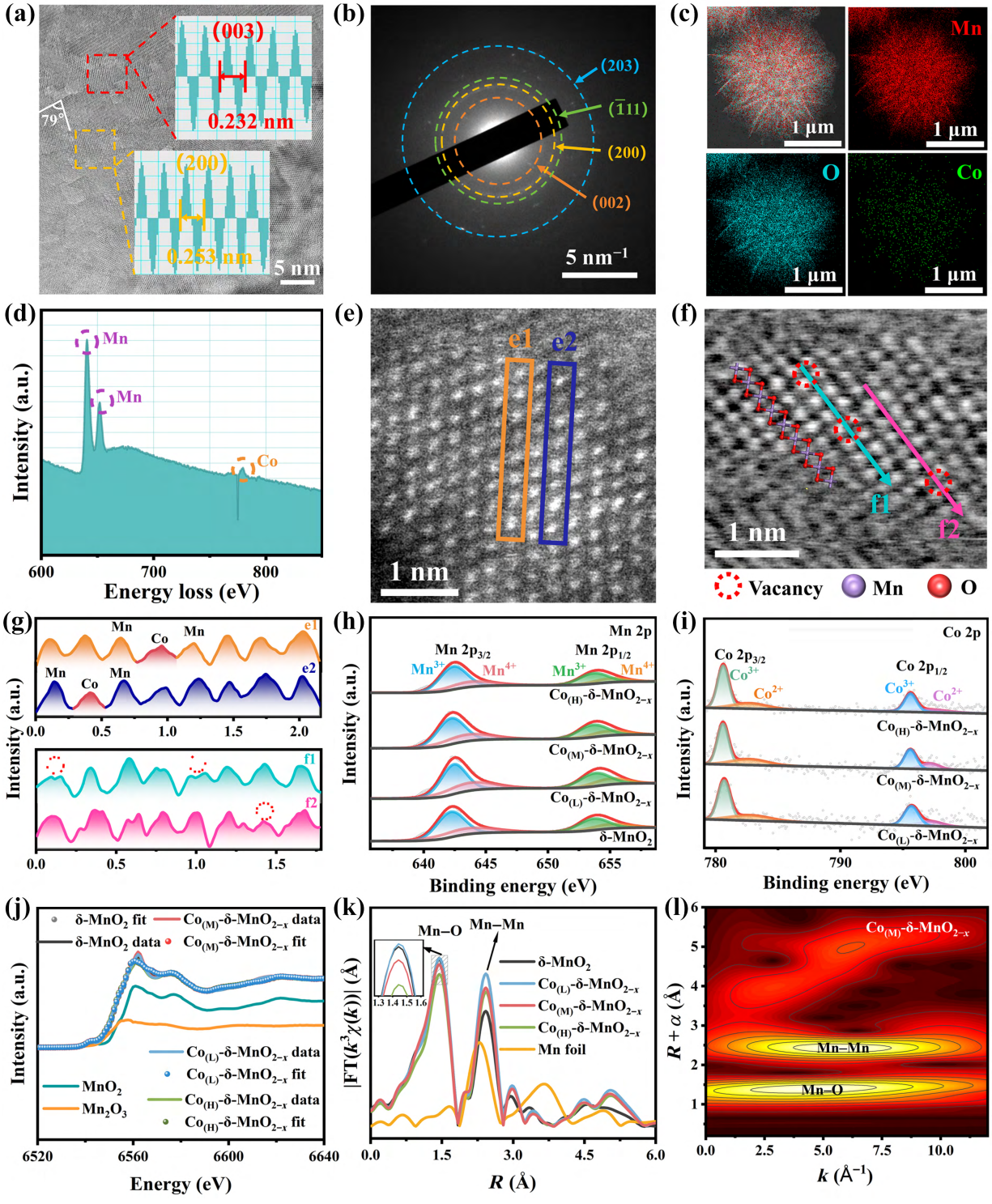

Figure 2 (a) HRTEM image, (b) SAED pattern, and (c) EDS elemental mappings of $Co_{(M)}$-δ-MnO_{2-x}. (d) EELS, (e) HAADF-STEM, and (f) ABF-STEM images of the prepared product. (g) The corresponding line intensity profiles extracted from orange area e1 and blue area e2 in (e) and ABF intensity profiles with inverse intensities along the lines indicated in (f). High-resolution XPS spectra of (h) Mn 2p and (i) Co 2p for δ-MnO_2, $Co_{(L)}$-δ-MnO_{2-x}, $Co_{(M)}$-δ-MnO_{2-x}, and $Co_{(H)}$-δ-MnO_{2-x}. (j) XANES and corresponding fitting plots at the Mn K-edge for δ-MnO_2, $Co_{(L)}$-δ-MnO_{2-x}, $Co_{(M)}$-δ-MnO_{2-x}, and $Co_{(H)}$-δ-MnO_{2-x}. (k) EXAFS spectra at the Mn K-edge for these samples. (l) WT-EXAFS plots at the Mn K-edge for $Co_{(M)}$-δ-MnO_{2-x}.

$2p_{3/2}$ signals of Mn^{4+}. Moreover, the two additional peaks at 655.5 and 644.2 eV correspond to the Mn $2p_{1/2}$ and Mn $2p_{3/2}$ of Mn^{3+} [23]. Notably, the Mn^{3+}/Mn^{4+} integral area ratio of δ-MnO_2, $Co_{(L)}$-δ-MnO_{2-x}, $Co_{(M)}$-δ-MnO_{2-x}, and $Co_{(H)}$-δ-MnO_{2-x} is gradually enhanced from 2.0 to 2.3, which manifests a reduction in the average manganese oxidation state induced by the alteration in the local electronic structure of δ-MnO_2 following Co incorporation [24]. Figure S55(k) in the ESM shows O 1s spectra, which exhibits three major peaks centered at 529.9, 531.7, and 533.2 eV, corresponding to metal–O, Mn–O–H, and H–O–H bonds, respectively [25]. The

O 1s peaks relating to lattice oxygen progressively shift to higher binding energies with the increase of Co substitution, possibly owing to the stronger electronegativity of Co heteroatoms that preserves lower electron cloud density around the O [26]. In terms of the deconvoluted high-resolution Co plots (Fig. 2(i)), the peaks centered at 782.7 and 797.2 eV are particularly characteristic of the $2p_{3/2}$ and $2p_{1/2}$ orbitals caused by the generation of Co–O bonds, and the binding energy at 780.6 and 795.6 eV are ascribed to Co^{3+}, and 782.7 and 797.2 eV can be assigned to Co^{2+}, which substantiates that the Co species are successfully introduced into the MnO_2 lattice [27]. Furthermore, an electron paramagnetic resonance (EPR) test was performed to investigate oxygen defects in the prepared samples. As displayed in Fig. S55(l) in the ESM, the characteristic peak of the Mn–O dangling bonds in $Co_{(L)}$-δ-MnO_{2-x}, $Co_{(M)}$-δ-MnO_{2-x} and $Co_{(H)}$-δ-MnO_{2-x} (g = 2.0, where g is the Landé g-factor) is significantly stronger compared to δ-MnO_2, demonstrating the existence of sufficient oxygen vacancies in the materials, which implies better electronic structure, more electroactive sites, and faster ion transport [28, 29]. In addition, X-ray absorption fine structure (XAFS) measurements at the Mn and Co K-edges were employed to further investigate the coordination geometries of the samples. The Mn K-edge X-ray absorption near edge structure (XANES) in Fig. S56(e) in the ESM reveals the coexistence of Mn^{3+} and Mn^{4+} for all obtained samples. For the sake of quantitatively ascertaining the proportion of each species, the linear combination fitting (LCF) approach was further adopted to perform the XANES spectra fitting, shown in Fig. 2(j) and Figs. S56(a)–S56(d) in the ESM [30]. Clearly, the Mn^{3+}/Mn^{4+} ratios were 0.94 for δ-MnO_2, 1.09 for $Co_{(L)}$-δ-MnO_{2-x}, 1.28 for $Co_{(M)}$-δ-MnO_{2-x}, and 1.39 for $Co_{(H)}$-δ-MnO_{2-x}, and the change tendencies is similar to those of XPS results. The Co K-edge XANES plots are close to each other, testifying that the substitution way preserves the negligible effect on the oxidation states of Co (Fig. S56(f) in the ESM). Figure 2(k) presents the k^2-weighted Fourier transformed (FT) profiles of the extended XAFS (EXAFS) displayed in R space for Mn K-edge. The prominent peaks centered at ~ 1.5 Å are attributed to Mn–O coordination state. In general, the peak intensity symbolizes the degree of disorder of atomic arrangement, and the smaller peak strength, the more defects or vacancies in the products [31]. A gradual decrease in the intensity of the peaks is achieved with the enhancement of Co species, obviously confirming the increased oxygen vacancy defects in δ-MnO_2 caused by the Co incorporation. Moreover, the Co K-edge FT-EXAFS spectra display a similar variation law in comparison to the R space for Mn K-edge, which reveals that partial oxygen vacancies also exist in Co–O configuration (Fig. S56(g) in the ESM). Besides, as a vital complement to FT-EXAFS, the enlarged wavelet transform (WT) contour maps were carried out as expressed in Fig. 2(l) and Figs. S56(h)–S56(m) in the ESM, respectively, which hold distinct resolutions in R space to further clarify the FT results. Therefore, the corresponding Mn–O and Co–O coordination environment of the fabricated δ-MnO_2, $Co_{(L)}$-δ-MnO_{2-x}, $Co_{(M)}$-δ-MnO_{2-x}, and $Co_{(H)}$-δ-MnO_{2-x} can be definitely observed in the visual WT images.

To investigate the variation in the electrochemical behavior of δ-MnO_2, $Co_{(L)}$-δ-MnO_{2-x}, $Co_{(M)}$-δ-MnO_{2-x}, and $Co_{(H)}$-δ-MnO_{2-x} as cathodes, the coin-type ZIBs were assembled employing a zinc foil, 2 M $ZnSO_4$ and 0.1 M $MnSO_4$ as anode and electrolyte, respectively, in the voltage range of 0.8–1.9 V (Fig. 3(a)). Figure S57(a) in the ESM shows the initial five cyclic voltammetry (CV) curves of $Co_{(M)}$-δ-MnO_{2-x} at a scan rate of 0.2 mV·s^{-1}, which exhibits two pairs of redox peaks at approximately 1.61/1.38 V and 1.58/1.24 V, indicating a multi-step Zn^{2+} deintercalation/intercalation [9]. Then, the prominent overlap of the CV plot shapes in subsequent cycles demonstrates that the redox reactions possess excellent electrochemical reversibility and stability. As displayed in Fig. 3(b) and Figs. S57(b)–S57(d) in the ESM, the typical anodic/cathodic CV peaks (marked as A1 and C1, respectively) of δ-MnO_2, $Co_{(L)}$-δ-MnO_{2-x}, $Co_{(M)}$-δ-MnO_{2-x}, and $Co_{(H)}$-δ-MnO_{2-x} are observed similarly at the scan rates ranging from 0.2 to 1.0 mV·s^{-1}. The $Co_{(M)}$-δ-MnO_{2-x} holds the narrowest voltage interval between the A1 and C1 peaks (≈ 335 mV at 1.0 mV·s^{-1}) as well as the strongest CV peak intensity among these samples (≈ 493, 420, and 409 mV at 1.0 mV·s^{-1}). The CV curves clearly indicate that the $Co_{(M)}$-δ-MnO_{2-x} cathode is absolutely advantageous in obtaining excellent structural stability, optimized polarization, and remarkable electrochemical reactivity [32, 33]. Figure S57(e) in the ESM illustrates the galvanostatic charge and discharge (GCD) plots of δ-MnO_2, $Co_{(L)}$-δ-MnO_{2-x}, $Co_{(M)}$-δ-MnO_{2-x}, and $Co_{(H)}$-δ-MnO_{2-x} at a current density of 0.5 A·g^{-1}. The GCD plot of $Co_{(M)}$-δ-MnO_{2-x} delivers both a sloping plateau (≈ 1.4 V, H^+ intercalation) and a flat plateau (≈ 1.3 V, Zn^{2+} intercalation) [34]. Similar two-step insertion reactions also appear in the δ-MnO_2, $Co_{(L)}$-δ-MnO_{2-x}, and $Co_{(H)}$-δ-MnO_{2-x}, the $Co_{(M)}$-δ-MnO_{2-x} cathode depicts the broadest discharge voltage plateau, implying the important improved electrochemical reactions. Meanwhile, the $Co_{(M)}$-δ-MnO_{2-x} cathode also distinctly exhibits the smallest over-potential gaps and the relatively maximum specific capacity in comparison with other as-synthesized cathodes, agreeing well with the CV results. The specific capacity and rate capability of these four cathodes are depicted in Fig. 3(c). Obviously, a series of average specific capacities of 655.7, 531.4, 414.7, 377.9, 348.5, 333.7, 283.6, 276.2, and 209.8 mAh·g^{-1} are achieved in $Co_{(M)}$-δ-MnO_{2-x} at 0.5, 1.0, 2.0, 3.0, 4.0, 5.0, 8.0, 10, and 20 A·g^{-1}, which are larger than those of other fabricated cathodes under the same parameters. The corresponding GCD plots also exhibit consistent electrochemical behaviors, which further substantiates the optimal capacity and rate capability characteristics for the $Co_{(M)}$-δ-MnO_{2-x} among these cathodes (Fig. 3(d) and Figs. S57(f)–S57(h) in the ESM). Significantly, the specific capacity and rate capability of the $Co_{(M)}$-δ-MnO_{2-x} cathode are superior to most of the reported manganese-based cathode materials in ZIBs (Fig. 3(e)) [9, 22, 34–40]. It is particularly noteworthy that the $Co_{(M)}$-δ-MnO_{2-x}//Zn displays a high energy density of 877.7 Wh·kg^{-1} at a power density of 0.67 kW·kg^{-1} and still holds 234.8 Wh·kg^{-1} even at 22.4 kW·kg^{-1}, which immensely surpasses the other as-prepared ZIBs with δ-MnO_2, $Co_{(L)}$-δ-MnO_{2-x}, and $Co_{(H)}$-δ-MnO_{2-x} cathodes (Fig. S57(i) in the ESM), as well as previously reported ZIBs as shown in Fig. 3(f) [22, 41–44]. Additionally, the specific capacity of the $Co_{(M)}$-δ-MnO_{2-x} cathode preserves no obvious attenuation at 0.5 A·g^{-1} after 150 cycles, while the specific capacity of the δ-MnO_2, $Co_{(L)}$-δ-MnO_{2-x}, and $Co_{(H)}$-δ-MnO_{2-x} rapidly declines to ~ 28%, 57%, and 33% of the initial capacity, respectively (Fig. S59(a) in the ESM). To further evaluate its excellent cycle stability, the $Co_{(M)}$-δ-MnO_{2-x} cathode is cycled at 5.0 A·g^{-1}. Surprisingly, a specific capacity of 303 mAh·g^{-1} is retained after 3500 cycles, corresponding to ~ 100% capacity retention rate, highlighting the superior cycling performance of the $Co_{(M)}$-δ-MnO_{2-x} cathode (Fig. 3(g) and Fig. S58 in the ESM). Compared with most related manganese-based materials reported in recent literature, such testing results have obvious advantages in cycle stability presented in Table S3 in the ESM. In order to further illustrate the potential applications of $Co_{(M)}$-

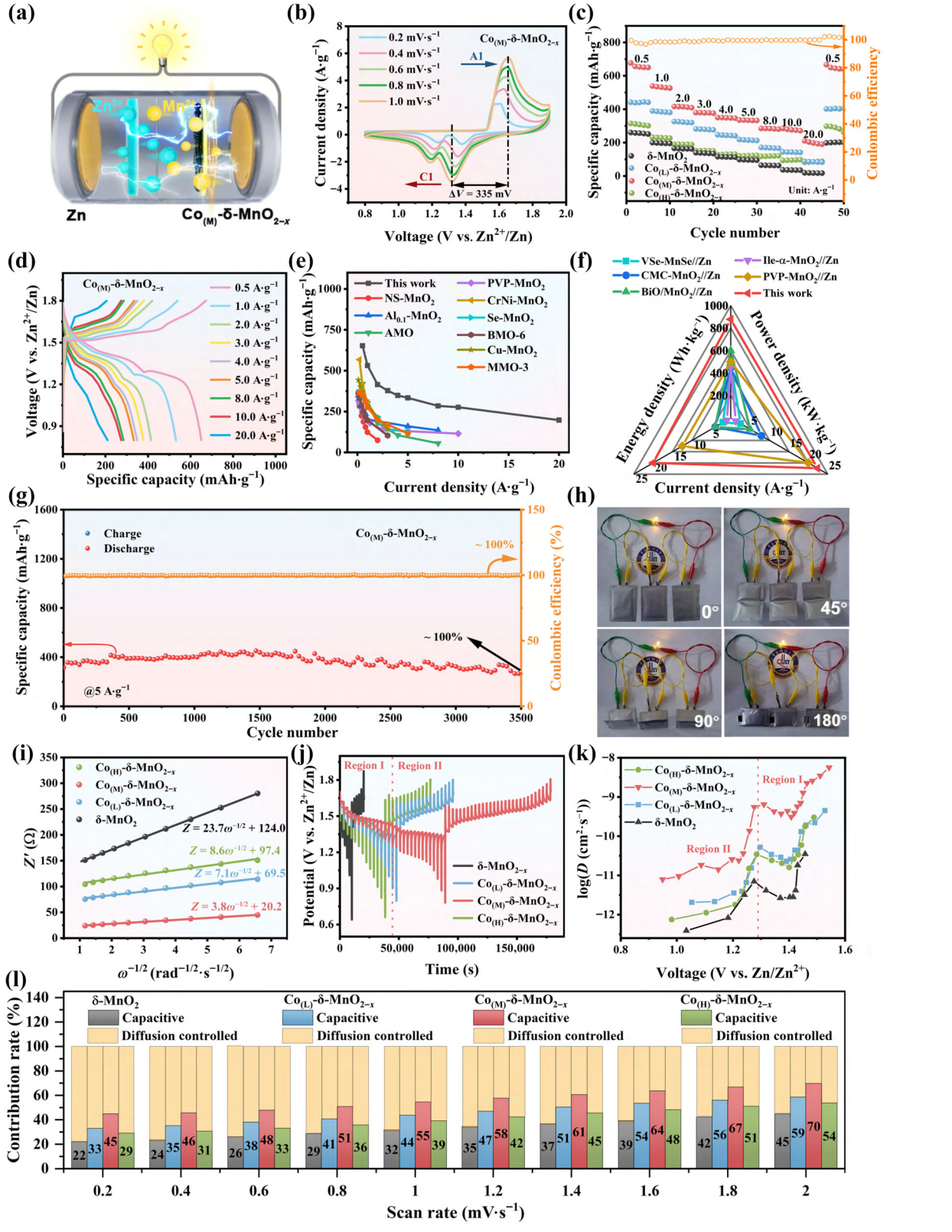

Figure 3 The electrochemical performances of δ-MnO_2, $Co_{(L)}$-δ-MnO_{2-x}, $Co_{(M)}$-δ-MnO_{2-x}, and $Co_{(H)}$-δ-MnO_{2-x} for coin-typed ZIBs. (a) Schematic configuration of $Co_{(M)}$-δ-MnO_{2-x}//Zn battery. (b) CV curves of $Co_{(M)}$-δ-MnO_{2-x} cathode at 0.2–1.0 mV·s^{-1}. (c) The rate capability comparison of these cathodes. (d) The GCD plots of $Co_{(M)}$-δ-MnO_{2-x} cathode at 0.5–20 A·g^{-1}. (e) Comparison of capacity and rate capability between $Co_{(M)}$-δ-MnO_{2-x} cathode and some state-of-the-art cathode materials for ZIBs. (f) Energy density and power density of the $Co_{(M)}$-δ-MnO_{2-x} cathode in comparison with previously reported manganese-based cathode materials for ZIBs. (g) Cycling stability of the prepared cathodes at 5 A·g^{-1}. (h) Photographs of the $Co_{(M)}$-δ-MnO_{2-x}//Zn battery illuminating a LED under the 0°, 45°, 90°, and 180° bending states. (i) The profiles of Z' versus $\omega^{-1/2}$ for δ-MnO_2, $Co_{(L)}$-δ-MnO_{2-x}, $Co_{(M)}$-δ-MnO_{2-x}, and $Co_{(H)}$-δ-MnO_{2-x} cathodes. (j) GITT plots and (k) Zn^{2+} diffusion coefficients of these cathodes. (l) Their normalized capacitive contribution ratios at various scan rates.

δ-MnO_{2-x} cathode, a light-emitting diode (LED) can be successfully lighted up by connecting two as-assembled ZIBs in series, whether bending at 0°, 45°, 90°, or 180°, as evidenced in Fig. 3(h), emphasizing the favorable flexibility and mechanical stability of the device. Based on the above experimental analysis, $Co_{(M)}$-δ-MnO_{2-x} shows the highest specific capacity and rate performance among the prepared cathodes, which adequately validates the predicted results of machine learning.

To systematically evaluate the reaction dynamics of δ-MnO_2, $Co_{(L)}$-δ-MnO_{2-x}, $Co_{(M)}$-δ-MnO_{2-x}, and $Co_{(H)}$-δ-MnO_{2-x} cathode during Zn^{2+} diffusion processes, electrochemical impedance spectroscopy (EIS), ultraviolet photoelectron spectroscopy (UPS), galvanostatic intermittence titration technique (GITT), and capacitive contribution measurements were carried out, as exhibited in Figs. 3(i)–3(l). Figure S59(b) in the ESM shows the EIS of δ-MnO_2, $Co_{(L)}$-δ-MnO_{2-x}, $Co_{(M)}$-δ-MnO_{2-x}, and $Co_{(H)}$-δ-MnO_{2-x} cathodes, and the corresponding equivalent circuit is fitted. The semicircle symbolizes the charge transfer impedance (R_{ct}), and the inclined line signifies the Warburg impedance (W_0) associated with the Zn^{2+} diffusion. The R_{ct} of $Co_{(M)}$-δ-MnO_{2-x} cathodes (10.61 Ω) is much smaller than those of δ-MnO_2 (70.57 Ω), $Co_{(L)}$-δ-MnO_{2-x} (29.37 Ω), and $Co_{(H)}$-δ-MnO_{2-x} (41.41 Ω), revealing the rapid charge transfer of $Co_{(M)}$-δ-MnO_{2-x} due to the boosted conductivity induced by the moderate Co doping. The correlation between the real part of the impedance (Z') and the inverse square root of the angular frequency ($\omega^{-1/2}$) of δ-MnO_2, $Co_{(L)}$-δ-MnO_{2-x}, $Co_{(M)}$-δ-MnO_{2-x}, and $Co_{(H)}$-δ-MnO_{2-x} was calculated according to Eq. (S12) in the ESM [45], shown in Fig. 3(i). The Warburg factor (σ) of the $Co_{(M)}$-δ-MnO_{2-x} is 3.8, which is much lower than those of δ-MnO_2 (23.7), $Co_{(L)}$-δ-MnO_{2-x} (7.1), and $Co_{(H)}$-δ-MnO_{2-x} (8.6), confirming that $Co_{(M)}$-δ-MnO_{2-x} exhibits the rapider ion diffusion rate. Moreover, the UPS and XPS valence band potential (E_{VB}) of the above cathodes are measured to assess their work function (Φ) and bandgap energy (E_g). The calculated Φ of δ-MnO_2, $Co_{(L)}$-δ-MnO_{2-x}, $Co_{(M)}$-δ-MnO_{2-x}, and $Co_{(H)}$-δ-MnO_{2-x} is 8.53, 8.24, 7.86, and 8.51 eV on the basis of Eq. (S13) in the ESM (Figs. S59(c)–S59(e) in the ESM) [46]. Excepted from the smaller Φ, from the E_{VB} and the corresponding conduction band potential (E_{CB}), the E_g of $Co_{(M)}$-δ-MnO_{2-x} is identified as 0.687 eV based on the equation of $E_{VB} = E_{CB} + E_g$, which is also lower than those of the other samples, contributing to higher electrical conductivity (Figs. S59(f)–S59(j) in the ESM). To further verify the rapid kinetic behavior, the GITT was performed at 0.5 $A \cdot g^{-1}$ to reach a 3 min pulse time with a rest time interval of 50 min for ascertaining the Zn^{2+} diffusion coefficient (D), as depicted in Fig. 3(j). The diffusion coefficient D can be obtained using Eq. (S14) in the ESM [11]. The result implies that the D values for the $Co_{(M)}$-δ-MnO_{2-x} cathode vary from 8.3×10^{-10} to 11.2×10^{-10} $cm^{-2} \cdot s^{-1}$ during charge process, which are higher than those of other as-prepared samples (Fig. 3(k)). Significantly, the D value of the $Co_{(M)}$-δ-MnO_{2-x} cathode in Region I is far superior to that in Region II. This discrepancy results from the smaller size of H^+ in comparison to Zn^{2+}, bringing about a lower energy barrier and diffusion impedance. It can be seen from the magnified view of each region that Region I exhibits smaller overvoltage and faster ion diffusion than Region II, indicating that the energy storage mechanism consists of the initial H^+ insertion and subsequent Zn^{2+} insertion (Fig. S59(k) in the ESM). Also, the reaction resistance of the $Co_{(M)}$-δ-MnO_{2-x} is minimum among these cathodes, which significantly promotes the charge transmission kinetics for efficient Zn^{2+} storage, as illustrated in Fig. S59(l) in the ESM. In addition, to understand whether Zn^{2+} transfer is dominated by capacitive control or diffusion control, CV plots of the as-fabricated cathodes at various scan rates from 0.2 to 2.0 $mV \cdot s^{-1}$ (Figs. S60(a)–S60(d) in the ESM) were further linearly fitted using the equation [47]: $i = av^b$, in which i and v stand for anodic/cathodic peak current and scan rates, respectively. a is adjustable parameters and b represents the constant (the slope value of the log$i$–log$v$ curve). As depicted in Figs. S60(e)–S60(h) in the ESM, the b values of Peaks 1, 2, 3, and 4 for $Co_{(M)}$-δ-MnO_{2-x} are 0.56, 0.55, 0.87, and 0.73, respectively, suggesting that the charge/discharge process is governed by a synergistic interaction between capacitive feature and diffusion behavior. In comparison to δ-MnO_2, $Co_{(L)}$-δ-MnO_{2-x}, and $Co_{(H)}$-δ-MnO_{2-x}, the larger b value of the $Co_{(M)}$-δ-MnO_{2-x} elucidates that capacitive-controlled procedure plays a primary role in determining the capacity and rate capability of this cathode, especially at the high scan rates, corroborating a rapid kinetics characteristic. The percentage of the Zn^{2+} capacitive contribution can be further quantified by separating i at a fixed potential into a capacitive influence (k_1v) and a diffusion control response ($k_2v^{1/2}$) using the equation [48]: $i = k_1v + k_2v^{1/2}$. The computed results reveal that the shaded region (purple) expresses a capacitive contribution of approximately 54.6% at 1.0 $mV \cdot s^{-1}$ for the $Co_{(M)}$-δ-MnO_{2-x} cathode (Fig. S60(i) in the ESM). More significantly, the capacitive-controlled contributions at various scan rates are also quantitatively determined, as shown in Fig. 3(l). The capacitive effect for $Co_{(M)}$-δ-MnO_{2-x} cathode gradually increases from 45% to 70% at varying scan rates from 0.2 to 2.0 $mV \cdot s^{-1}$, which is even higher than those of the δ-MnO_2, $Co_{(L)}$-δ-MnO_{2-x}, and $Co_{(H)}$-δ-MnO_{2-x} cathodes at the different scan rates, illustrating enhanced capacitive behavior and accelerated Zn^{2+} migration kinetics following the optimal cobalt substitution.

DFT calculations were performed to unlock the fundamental reasons for faster redox kinetics and superior rate capability of $Co_{(M)}$-δ-MnO_{2-x} in comparison to other as-synthesized cathodes, as illustrated in Fig. 4. Based on the model diagrams of δ-MnO_2 adsorbing Zn^{2+} and Co-doped δ-MnO_2 adsorbing Zn^{2+} (Fig. S61 in the ESM), the corresponding Zn^{2+} adsorption energy (E_{ads}) on different sites of Mn1, Mn2, Co, and OV were calculated shown in Fig. 4(a). In general, as for the ion insertion/extraction process, the adsorption energy should neither be too strong nor too weak. Namely, at the adsorption sites with overall stronger adsorption ability, the optimal candidate should exhibit relatively weaker adsorption strength, and *vice versa*. Obviously, from Fig. 4(a), only the $Co_{(M)}$-δ-MnO_{2-x} satisfies the aforementioned rules among these samples, preliminarily revealing that the $Co_{(M)}$-δ-MnO_{2-x} configuration has the most suitable adsorption of Zn^{2+}, which may make it a superior cathode. Moreover, d-band center (ε_d) and Gibbs free energy change (ΔG) were also calculated according to those model diagrams (Figs. S62 and S63 in the ESM). As displayed in Fig. 4(b), the d-band center progressively shifts closer to the Fermi level (0 eV) with the increase of Co doping ratio, indicating an enhancement of the chemical binding energy between the cathode materials and Zn^{2+}. Thus, the $Co_{(H)}$-δ-MnO_{2-x} owns the highest ε_d, resulting in a robust binding ability of Zn^{2+}. Theoretically, the $Co_{(H)}$-δ-MnO_{2-x} cathode holds prominent electrochemical performances; nevertheless, the $Co_{(M)}$-δ-MnO_{2-x} cathode presents the largest specific capacity and rate capability in practice. This is because exceedingly steady Zn^{2+} binding strength involving the $Co_{(H)}$-δ-MnO_{2-x} may give rise to more troubles for the Zn^{2+} extraction during the charge process than that of the $Co_{(M)}$-δ-MnO_{2-x}, leading

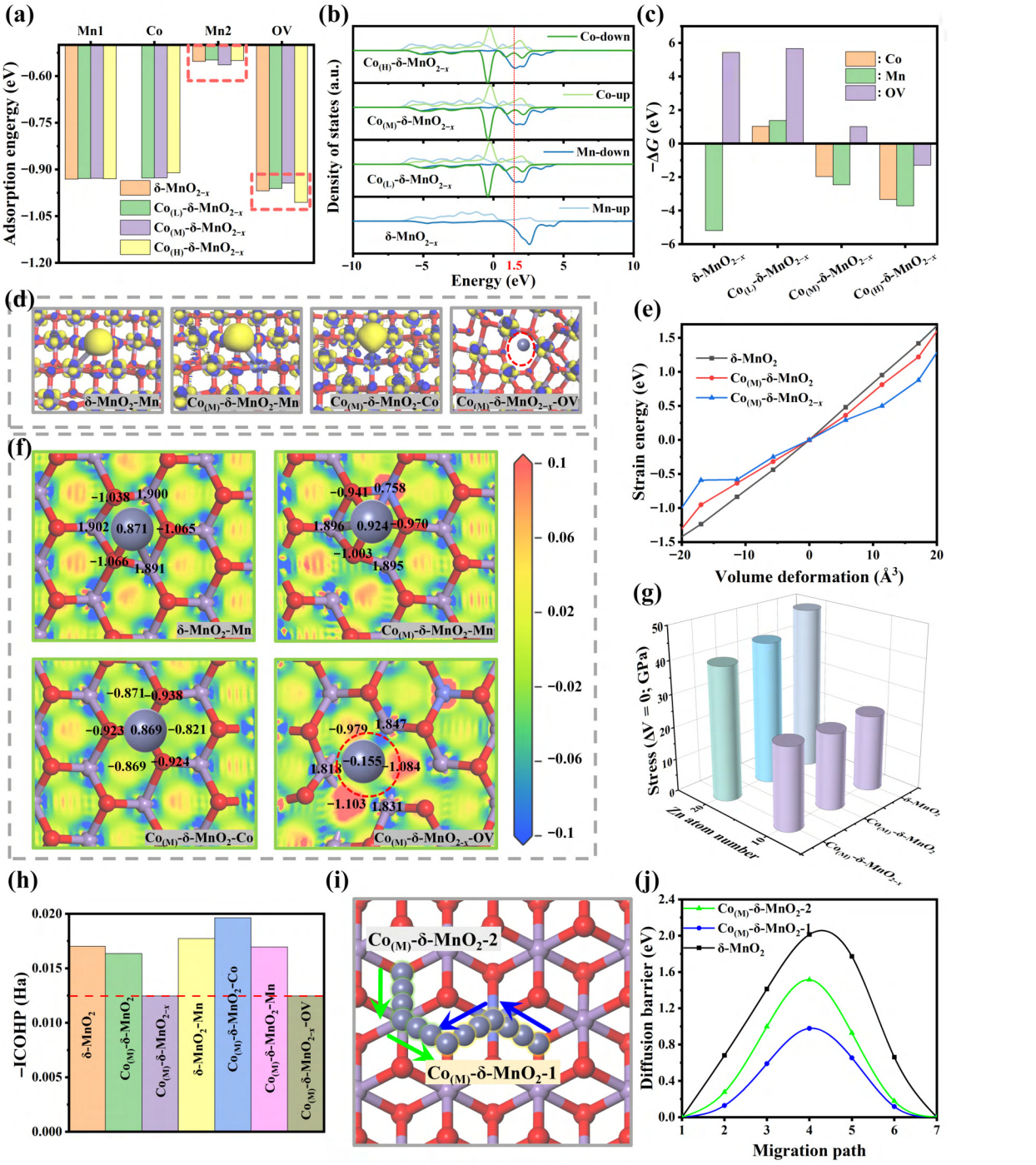

Figure 4 DFT calculations of these fabricated cathodes. (a) The adsorption energies of δ-MnO_{2-x} adsorbing zinc ions and Co-doped δ-MnO_{2-x} adsorbing zinc ions, and (b) the corresponding d-band center. (c) Gibbs free energy of charging storage on the synthesized samples. (d) The differential charge density maps of δ-MnO_2 and $Co_{(M)}$-δ-MnO_{2-x} with Zn^{2+} adsorption on the different sites (red dashed lines represent OVs) and (f) the corresponding charge density distribution plots. (e) Strain energy–volume deformation curves of δ-MnO_2, $Co_{(M)}$-δ-MnO_2, and $Co_{(M)}$-δ-MnO_{2-x}. (g) Comparison of the interior stress between δ-MnO_2, $Co_{(M)}$-δ-MnO_2, and $Co_{(M)}$-δ-MnO_{2-x} versus the different Zn atom number. (h) –ICOHP of Mn–O bonds in δ-MnO_2, $Co_{(M)}$-δ-MnO_2, $Co_{(M)}$-δ-MnO_{2-x}, and these samples adsorbing Zn^{2+} on different sites. (i) The Zn^{2+} migration paths in $Co_{(M)}$-δ-MnO_2 and (j) the comparison for Zn^{2+} diffusion energy barrier of δ-MnO_2 and $Co_{(M)}$-δ-MnO_2.

to extraordinary inferior reversibility of the $Co_{(H)}$-δ-MnO_{2-x}. Also, we discussed the Δ*G* on various sites to investigate the influences of the introduced Co concentration on redox activities (Fig. 4(c)). Clearly, as for δ-MnO_2, $Co_{(L)}$-δ-MnO_{2-x} and $Co_{(H)}$-δ-MnO_{2-x}, either the Zn^{2+} desorption or adsorption is difficult. Fortunately, the $Co_{(M)}$-δ-MnO_{2-x} possesses a moderate Zn^{2+} adsorption/desorption capability; thus, it can deliver the optimal oxidation/reduction equilibrium, greatly boosting the reversible charge storage and preserving a desired redox reaction activity. According to the above calculated results, the produced Co ratio in the cathode materials holds an optimal level rather than a limitlessly enhanced Co concentration. Consequently, our study offers an effective strategy for identifying the optimal heteroatom concentration, which is of enormous significance for exploiting high-performance ZIBs

cathode materials. Furthermore, to further disclose the roles of the moderate Co content on the reversibility and structural stability of the cathode, differential charge density and the corresponding charge density distribution, strain energy versus volume deformation, COHP of δ-MnO_2, $Co_{(M)}$-δ-MnO_2, and $Co_{(M)}$-δ-MnO_{2-x} were conducted (the related model diagrams shown in Figs. S64–S66 in the ESM), as depicted in Figs. 4(d)–4(h). The electronic interactions between the δ-MnO_2, $Co_{(M)}$-δ-MnO_2, $Co_{(M)}$-δ-MnO_{2-x}, and the adsorbed Zn^{2+} are illustrated through the charge density difference analysis (Fig. 4(d)). An evident charge accumulation–depletion area can be achieved at the interface between Zn^{2+} and the tightly neighboring active materials with Mn, Co, and OV sites, confirming charge redistribution during the redox reactions. Notably, the typical chemical adsorption types on the Mn and Co sites are clearly determined, while the Zn^{2+} adsorption on the OV sites belongs to the physical species. Simultaneously, in order to confirm it more visually, we also quantified the Mulliken charge density distribution for adjacent atoms (Fig. 4(f)). Compared with the Mn sites in δ-MnO_2 (with Mulliken charge of 0.871e), the Mn sites in the $Co_{(M)}$-δ-MnO_2 (with Mulliken charge of 0.924e) can strongly adsorb Zn^{2+}, while the Mulliken charge of Co sites in the $Co_{(M)}$-δ-MnO_2 is only 0.869 e. This configuration contributes to forming a typical alternation potential field with "strong anchoring sites" and "weak transition sites", which makes Mn sites in the $Co_{(M)}$-δ-MnO_2 firmly capture Zn^{2+} to ensure the structure stability. The Co sites can act as a low potential barrier area, effectively reducing the Zn^{2+} desorption difficulty. The periodic fluctuation of the binding energy enables Zn^{2+} to cross the lower energy barriers, and spontaneously slides from the weak sites to the strong sites using the energy difference and easily migrates to the next position. Thus, it not only guarantees the adsorption capacity but also significantly reduces the migration energy barrier, greatly improving the surface diffusion efficiency. Figure 4(e) displays the strain energy–volume deformation plots of δ-MnO_2, $Co_{(M)}$-δ-MnO_2, and $Co_{(M)}$-δ-MnO_{2-x}. Clearly, the curve of $Co_{(M)}$-δ-MnO_{2-x} delivers a much smaller slope than those of the δ-MnO_2 and $Co_{(M)}$-δ-MnO_2, revealing that the formed stress level in the $Co_{(M)}$-δ-MnO_{2-x} is much lower versus the counterpart of the δ-MnO_2 and $Co_{(M)}$-δ-MnO_2, which is well agreement with the calculated bond lengths result (Fig. S67 in the ESM). More importantly, with increasing the inserted Zn^{2+} number ranging from 10 to 20, the enhanced interior stress for $Co_{(M)}$-δ-MnO_{2-x} (15.5 GPa) is the lowest among these cathodes (δ-MnO_2, 26.3 GPa. $Co_{(M)}$-δ-MnO_2, 20.1 GPa), vindicating the sufficiently alleviated mechanical strains within the $Co_{(M)}$-δ-MnO_{2-x} structure after moderate Co substitution (Fig. 4(g)). This can contribute to facilitating the stable charge and discharge of $Co_{(M)}$-δ-MnO_{2-x} due to its superior strain-relieved characteristics. COHP analysis is further utilized to ascertain the bonding stability of the cathode materials and their Zn^{2+}-intercalated phases. The corresponding results and calculated −ICOHP values are shown in Fig. S68 in the ESM and Fig. 4(h), respectively. Although −ICOHP of $Co_{(M)}$-δ-MnO_2 is similar to the δ-MnO_2 and $Co_{(M)}$-δ-MnO_{2-x}, the structural stability of the $Co_{(M)}$-δ-MnO_2 system can be enhanced by introducing Zn^{2+}, leading to higher −ICOHP values of 4.8. According to Zn^{2+} adsorption behavior and bonding thermodynamics analyses, the creation of Co heteroatoms can help δ-MnO_2 to trap Zn^{2+} and form a thermodynamically stable $Co_{(M)}$-δ-MnO_2 phase, effectively increasing the structural integration of the evolutional active materials. The unique integrated features can effectively prevent the architecture collapse or pulverization caused by the Zn^{2+} insertion/extraction, especially at high current density, significantly improving the rate capability and cycling performance of the ZIBs cathode. In addition, the Zn^{2+} diffusion processes within the δ-MnO_2 and $Co_{(M)}$-δ-MnO_2 structures were simulated (Figs. 4(i)–4(j) and Fig. S69 in the ESM). As a comparison, the lowest Zn^{2+} migration energy barriers can be obtained after Co substitution along the diffusion path 1 (around the Co atoms), which is conducive to the Zn^{2+} diffusion kinetics, thus giving rise to the outstanding rate capability of $Co_{(M)}$-δ-MnO_2.

Notably, to optimize the prediction models of ZIBs cathode performance, it is necessary to screen out the crucial material parameters that are sensitive to doping and directly related to electrochemical properties. DFT calculations confirmed that the electronic structure features, such as pDOS, COOP, and COHP, change significantly with the doping concentration, which can be used as effective input variables for predicting rate performance and specific capacity of the cathodes in machine learning. Meanwhile, physical properties tightly associated with electrochemical kinetics, including adsorption energy, chemical bonding energy, and Gibbs free energy, are also highly sensitive to the heteroatom doping, and their variations can exert an important impact on the Zn^{2+} migration energy barrier. Thus, incorporating these parameters with clear physical meanings into the models is the core strategy for breaking through the current bottleneck in predicting the accuracy and enhancing the interpretability of the models.

To gain deep insights into the reaction mechanism of $Co_{(M)}$-δ-MnO_{2-x} cathode in ZIBs, *ex-situ* XRD, XPS, SEM, and TEM were adopted to determine the changes of structure and composition during the charge/discharge process (Fig. 5). Based on the initial GCD plot at 0.5 $A{\cdot}g^{-1}$ (Fig. 5(a)), several significant states (States I–XVI) that correspond to the points in the charge/discharge curves are chosen for *ex-situ* XRD measurements presented in Figs. 5(b) and 5(c). Four diffraction peaks at around 26.2°, 42.2°, 44.4°, and 54.0° are assigned to the graphene substrate. The initial state (State I) corresponds to the as-prepared $Co_{(M)}$-δ-MnO_{2-x} cathode, showing diffraction peaks consistent with the powder sample along with characteristic peaks of the graphene substrate. During the discharge process (States II–IX), new diffraction peaks emerged at 12.4°, 21.8°, 41.6°, 47.8°, and 69.9° in the XRD patterns, which are examined as zinc sulfate hydroxide (ZSH, $Zn_4SO_4(OH)_6{\cdot}0.5H_2O$, PDF No. 00-044-0674 and $Zn_4SO_4(OH)_6{\cdot}3H_2O$, PDF No. 00-039-0689). This is the consequence of H^+ consumption leading to OH^- accumulation in the electrolyte, generating an alkaline situation in which redundant OH^- interacts with Zn^{2+} and SO_4^{2-} to form ZSH [49]. Apart from the peaks of ZSH, the typical peaks of the $ZnMn_2O_4$ (ZMO, PDF No. 97-001-5305) phase centered at 33.1°, 36.4°, 59.0°, and 65.1° are ascertained during the discharge process (States V–IX) caused by the Zn^{2+} intercalation. As the discharge depth reaches 0.80 V (State IX), the intensity of the ZSH and ZMO diffraction peaks enhances further [50]. Notably, during subsequent charging (from State IX to State XVI), the diffraction peaks of these byproducts weaken and disappear gradually, suggesting the occurrence of a reversible dissolution/deposition process for ZSH [38, 50, 51]. The reversible structural evolution process illustrates the reversible insertion/extraction behavior of Zn^{2+} and H^+ in the cathode, confirming the remarkable electrochemical reversibility of the $Co_{(M)}$-δ-MnO_{2-x}. The energy storage mechanism of $Co_{(M)}$-δ-MnO_{2-x} cathode during the initial charge and discharge cycle can be systematically expounded as follows

$$MnO_2 + 4H^+ + 2e^- \rightleftharpoons 2H_2O + Mn^{2+} \quad (1)$$

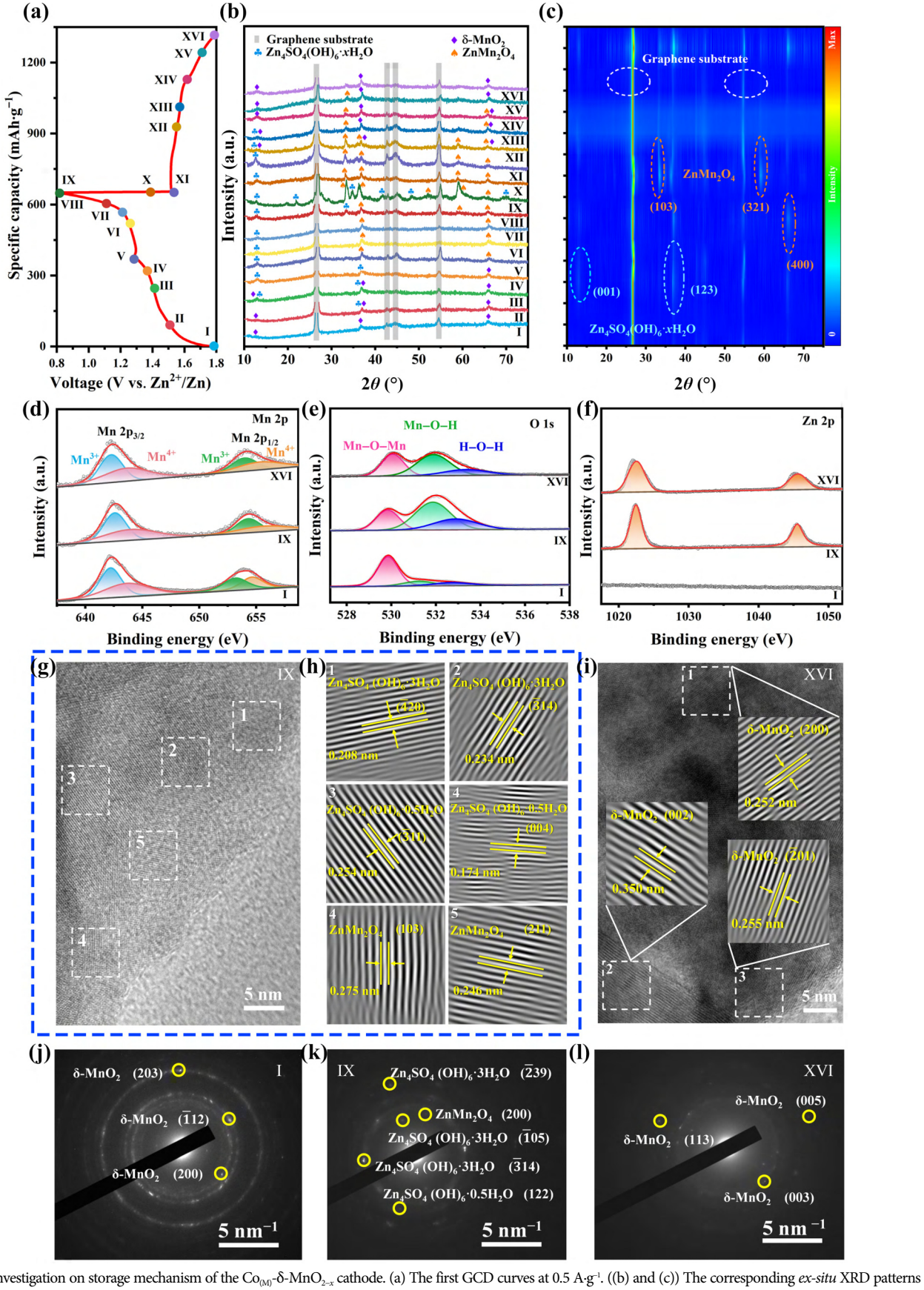

Figure 5 Investigation on storage mechanism of the $Co_{(M)}$-δ-MnO_{2-x} cathode. (a) The first GCD curves at 0.5 A·g^{-1}. ((b) and (c)) The corresponding *ex-situ* XRD patterns with a 2D contour plot of the series of selected states during the discharge/charge process. *Ex-situ* XPS spectra of (d) Mn 2p, (e) O 1s, and (f) Zn 2p at different charge/discharge stages. ((g)–(i)) *Ex-situ* HRTEM images and ((j)–(l)) SAED plots at various states within the first cycle.

$$4Zn^{2+} + 6OH^- + ZnSO_4 + xH_2O \rightleftharpoons Zn_4(OH)_6SO_4 \cdot xH_2O \quad (2)$$

$$Zn^{2+} + 2e^- + 2MnO_2 \rightleftharpoons ZnMn_2O_4 \quad (3)$$

Moreover, the *ex-situ* XPS plots were conducted to further elucidate the phase evolution process, with the result in Figs. 5(d)–5(f). In terms of Mn 2p (Fig. 5(d)), when gradually discharging to 0.8 V, much lower oxide state of Mn (Mn^{3+}/Mn^{4+}) took place, which is ascribed to the generation of Zn_xMnO_2 induced by the Zn^{2+} insertion. After charging back to 1.8 V, the oxide state of Mn progressively augmented, indicating that the Zn^{2+} has successfully extracted [52]. Meanwhile, from the O 1s spectra, there existed distinct phase evolution on ZSH during the discharge and charge process (Fig. 5(e)). Other than, as shown in Fig. 5(f), no Zn signal is tracked in the initial status without charge and discharge. However, at the first discharge to 0.8 V (State IX), the characteristic peak signals referring to the Zn 2p spectrum were monitored, located at 1022.5 and 1045.5 eV, manifesting that the Zn^{2+} intercalation reaction appeared and produced Zn_xMnO_2. When charged to 1.8 V, the Zn signal intensity reduces remarkably, implying that numerous Zn^{2+} have been extracted from the lattice. The maintained attenuated Zn signal peak is possibly a result of the residual adsorption of Zn^{2+} on the cathode surface [52]. In addition, the observations of *ex-situ* SEM and *ex-situ* TEM images are identical to the XRD results and further substantiate the reversible micro-morphology evolution (Fig. S70 in the ESM). During discharge, thick and rough sheet-like structures are apparently detected, demonstrating the formation of ZSH. Upon charging, ZSH gradually decomposes, and the flower-like nanospheres composed of many interconnected nanosheets have appeared again after full charge (State XVI), further validating the excellent reversibility of the ZSH during cycling. It can be seen from *ex-situ* HRTEM and SAED images, at the original State I, the observed lattice fringes are assigned to δ-MnO_2 phase (Fig. S71 in the ESM and Fig. 5(j)). When discharged to the State IX, the lattice fringes clearly correspond to $(\bar{4}20)$ and $(\bar{3}14)$ crystal planes of $Zn_4SO_4(OH)_6{\cdot}3H_2O$, $(\bar{3}11)$ and (004) crystal planes of $Zn_4SO_4(OH)_6{\cdot}0.5H_2O$, and (103) and (211) crystal planes of $ZnMn_2O_4$, which are well matched with the characteristic diffraction rings observed in SAED (Figs. 5(g), 5(h), and 5(k)). It indicates that the insertion of H^+/Zn^{2+} has generated $Zn_4SO_4(OH)_6{\cdot}xH_2O$ and $ZnMn_2O_4$. In contrast, when the cathode is situated at State XVI, the characteristic lattice fringes and diffraction rings evidently depict the crystal planes of δ-MnO_2, substantially recovering to the initial byproducts (Figs. 5(i) and 5(l)). The typical redox mechanisms and highly reversible behaviors during the discharge/charge process play critical roles in improving capacity and rate performance of the as-obtained cathode.

Relevant data and code are publicly available at https://github.com/jyjpxby/zinc-ion-battery.git.

3 Conclusions

In summary, we configure the optimal heteroatom species and concentration in δ-MnO_2, and yield qualitative "structure–activity" descriptor via employing an innovative research paradigm combining machine learning predictions, DFT simulations and systematic experiments, affording a targeted design strategy for high-performance doped-δ-MnO_2 cathode materials. More importantly, for the first time, we systematically simulate the two quantitative indicators of binding energy gradient distribution and activation area ratio from a two-dimensional perspective to fundamentally unlock the prediction mechanism of machine learning and reliably pledge its accuracy. Building upon this understanding, we designed the $Co_{(M)}$-δ-MnO_{2-x} cathode material, which delivers a high specific capacity of 655.7 mAh·g^{-1} at 0.5 A·g^{-1}, superior rate performance (209.8 mAh·g^{-1} at a high current density of 20 A·g^{-1}), and outstanding cycling stability, surpassing those of previously reported manganese-based cathodes. With the combination of DFT calculations, electrochemical test, and *ex-situ* structural analysis, the superb performance of $Co_{(M)}$-δ-MnO_{2-x} is attributed to the suitable adsorption energy/Gibbs free energy, a higher –ICOHP, along with a lower Zn^{2+} diffusion barrier to enable Zn^{2+} adsorption–desorption equilibrium and significantly accelerate reaction kinetics. In this regard, our work can not only provide conceptual, material, and technical breakthroughs for developing high-performance manganese-based ZIBs cathodes, but also extend to other energy storage and conversion layered materials in the future.

Electronic Supplementary Material: Supplementary material (machine learning and DFT calculations, calculating formula, and experimental section) is available in the online version of this article at https://doi.org/10.26599/NR.2026.94908928.

Data availability

All data needed to support the conclusions in the paper are presented in the manuscript and the Electronic Supplementary Material. Additional data related to this paper may be requested from the corresponding author upon request.

Acknowledgements

The work reported here was supported by the National Natural Science Foundation of China (Nos. 22379081 and 22379080) and the Natural Science Foundation of Shandong Province under Grant (No. ZR2023QE059).

Declaration of competing interest

All the contributing authors report no conflict of interests in this work.

Author contribution statement

J. Z. (Jian Zhao), R. Y. L., and Z. J. L. put forward the idea and designed the research. Y. T. D., Y. J. J., and W. L. contributed equally to this work. Y. T. D., W. L., B. X., and J. Z. W. performed the cathode material preparation, characterization, and electrochemical measurement. Y. T. D., W. Y. L., G. H. C., X. K. W., and T. L. contributed to the electrochemical analysis. Y. J. J., J. Z. (Jing Zhang), and X. Q. G. carried out the machine learning technique and DFT calculations. Y. T. D., Y. J. J., D. H. C., Y. W. S., V. B., H. B., and E. C. conducted the data analysis and mechanism discussion. Y. T. D. and Y. J. J. drafted the manuscript with input from all authors. J. Z. (Jian Zhao), R. Y. L., Z. J. L., Y. W. S., E. C., and X. K. W. offered major revisions. All authors discussed the results and contributed to the manuscript. All the authors have approved the final manuscript.

Use of AI statement

None.

References

[1] Song, H. B.; Cui, Y. F.; Li, Y. F.; Li, X. L.; Li, Y. X.; Zhao, N.; Li, W. J.; Wu, C.; Xi, S. B.; Huang, S. Z. et al. Alcohol molecule coupling: A universal approach to modulating amorphousness in vanadium-based cathodes for high-rate and durable aqueous zinc-ion batteries. *Sci. Adv.* **2025**, *11*, eadt7502.

[2] Lin, D. W.; Li, J. P.; Wang, M. Z.; Jian, M. Q.; Pan, R. H.; Liu, Y.; Zhu, A. Q.; Zhang, T.; Liu, K.; Feng, D. Y. et al. Nanofluidic-engineered carbon nanotube ion highways in hydrogels enable high-power aqueous zinc-ion batteries. *Sci. Adv.* **2025**, *11*, eadx9812.

[3] Zhang, T.; Li, T.; Shen, Y.; Ma, H. X.; Wei, C. Y.; Cai, J. H.; Xu, Y.; Li, Y. Y.; Dong, X. J.; Zhang, S. C. et al. Enhanced kinetics and stability of Zn–MnO_2 batteries with a multifunctional TiO_2 coating. *Adv. Mater.* **2025**, *37*, 2505082.

[4] Lai, G. J.; Zhao, Z. Q.; Zhang, H.; Hu, X. T.; Lu, B. G.; Liang, S. Q.; Zhou, J. *In-situ* positive electrode–electrolyte interphase construction enables stable Ah-level Zn–MnO_2 batteries. *Nat. Commun.* **2025**, *16*, 2194.

[5] Chen, Y.; Lin, C. Z.; Chen, X.; Lu, Z. H.; Zhang, K. C.; Liu, Y.; Wang, J. N.; Han, G. R.; Xu, G. Modulating the structure of interlayer/layer matrix on δ-MnO_2 via cerium doping-engineering toward high-performance aqueous zinc ion batteries. *Adv. Energy Mater.* **2024**, *14*, 2304303.

[6] Xiong, T.; Zhang, Y. X.; Lee, W. S. V.; Xue, J. M. Defect engineering in manganese-based oxides for aqueous rechargeable zinc-ion batteries: A review. *Adv. Energy Mater.* **2020**, *10*, 2001769.

[7] Wang, S. J.; Guo, X.; Huang, K.; Achari, A.; Safaei, J.; Lei, Y. J.; Li, D. F.; Gu, Q. F.; Sun, C. H.; Gloag, L. et al. Cooperative Jahn–Teller effect and engineered long-range strain in manganese oxide/graphene superlattice for aqueous zinc-ion batteries. *Nat. Commun.* **2025**, *16*, 5191.

[8] Tang, H.; Yao, J. J.; Zhu, Y. R. Recent developments and future prospects for zinc-ion hybrid capacitors: A review. *Adv. Energy Mater.* **2021**, *11*, 2003994.

[9] Yao, H. X.; Yu, H.; Zheng, Y. Q.; Li, N. W.; Li, S.; Luan, D. Y.; Lou, X. W.; Yu, L. Pre-intercalation of ammonium ions in layered δ-MnO_2 nanosheets for high-performance aqueous zinc-ion batteries. *Angew. Chem., Int. Ed.* **2023**, *62*, e202315257.

[10] Li, W. B.; Song, Q. Q.; Dong, Q.; Zhang, J. H.; Wang, J. J.; Wu, Y. M.; Yu, Y.; Li, X. F. Proton storage chemistry in aqueous zinc-inorganic batteries with moderate electrolytes. *Adv. Mater.* **2025**, *37*, 2414019.

[11] Li, S. J.; Xu, X. Y.; Chen, W. X.; Zhao, J. W.; Wang, K.; Shen, J. S.; Chen, X.; Lu, X.; Jiao, X. X.; Liu, Y. Y. et al. Synergetic impact of oxygen and vanadium defects endows $NH_4V_4O_{10}$ cathode with superior performances for aqueous zinc-ion battery. *Energy Storage Mater.* **2024**, *65*, 103108.

[12] Zuo, C. L.; Xiong, F. Y.; Shao, Y. H.; Li, M.; Zhu, D. Y.; Zhu, J. X.; Wang, J.; An, Q. Y. Mitigating Jahn–Teller effect of MnO_2 via charge regulation of Mn-local environment for advanced calcium storage. *Energy Storage Mater.* **2024**, *72*, 103763.

[13] Lu, S. H.; Zhou, Q. H.; Ouyang, Y. X.; Guo, Y. L.; Li, Q.; Wang, J. L. Accelerated discovery of stable lead-free hybrid organic–inorganic perovskites via machine learning. *Nat. Commun.* **2018**, *9*, 3405.

[14] Han, Z. Y.; Chen, A.; Li, Z. J.; Zhang, M. T.; Wang, Z. L.; Yang, L. X.; Gao, R. H.; Jia, Y. Y.; Ji, G. J.; Lao, Z. J. et al. Machine learning-based design of electrocatalytic materials towards high-energy lithium||sulfur batteries development. *Nat. Commun.* **2024**, *15*, 8433.

[15] Xu, Y. H.; Zhang, G. N.; Wang, X. X.; Zhang, J. H.; Wen, H. C.; Wang, D. N.; Yuan, Y. T.; Jiang, Q. T.; Qian, H. M.; Xi, Y. K. et al. Efficient modulation d/p-band center proximity in birnessite-type MnO_2 by cation/anion co-doping for enhanced dual-ion storage. *Adv. Funct. Mater.* **2025**, *35*, 2500137.

[16] Fan, W. J.; Tian, S. Y.; Qin, L. P.; Alomar, T. S.; Ruan, P. C.; El-Bahy, Z. M.; AlMasoud, N.; Lu, B. G.; Zhou, J. Inner-sphere electron transfer enabling highly reversible Mn^{2+}/MnO_2 conversion toward energy-dense electrolytic zinc-manganese batteries. *J. Am. Chem. Soc.* **2025**, *147*, 18694–18703.

[17] Khan, S. T.; Moosavi, S. M. Connecting metal–organic framework synthesis to applications using multimodal machine learning. *Nat. Commun.* **2025**, *16*, 5642.

[18] Fujii, S.; Shimizu, Y.; Hyodo, J.; Kuwabara, A.; Yamazaki, Y. Discovery of unconventional proton-conducting inorganic solids via defect-chemistry-trained, interpretable machine learning. *Adv. Energy Mater.* **2023**, *13*, 2301892.

[19] Wang, G. Y.; Fearn, T.; Wang, T. Y.; Choy, K. L. Machine-learning approach for predicting the discharging capacities of doped lithium nickel-cobalt-manganese cathode materials in Li-ion batteries. *ACS Cent. Sci.* **2021**, *7*, 1551–1560.

[20] Liow, C. H.; Kang, H.; Kim, S.; Na, M.; Lee, Y.; Baucour, A.; Bang, K.; Shim, Y.; Choe, J.; Hwang, G. et al. Machine learning assisted synthesis of lithium-ion batteries cathode materials. *Nano Energy* **2022**, *98*, 107214.

[21] Cai, J. F.; Wang, Z. L.; Wu, S. C.; Han, Y. Q.; Li, J. J. A Machine learning shortcut for screening the spinel structures of Mg/Zn ion battery cathodes with a high conductivity and rapid ion kinetics. *Energy Storage Mater.* **2021**, *42*, 277–285.

[22] Zhang, A. Q.; Zhao, R.; Wang, Y. H.; Yue, J. S.; Yang, J. J.; Wang, X. R.; Wu, C.; Bai, Y. Hybrid superlattice-triggered selective proton grotthuss intercalation in δ-MnO_2 for high-performance zinc-ion battery. *Angew. Chem., Int. Ed.* **2023**, *62*, e202313163.

[23] Liu, L. Y.; Wu, Y. C.; Huang, L.; Liu, K. S.; Duployer, B.; Rozier, P.; Taberna, P. L.; Simon, P. Alkali ions pre-intercalated layered MnO_2 nanosheet for zinc-ions storage. *Adv. Energy Mater.* **2021**, *11*, 2101287.

[24] Li, T. T.; Zhang, N.; Liu, B. C.; Wang, P. F.; Liu, Z. L.; Wang, Y. G.; Xu, D. H.; Tian, H.; Zhang, Q. Y.; Yi, T. F. Unlocking the critical role of cations doping in MnO_2 cathode with enhanced reaction kinetics for aqueous zinc ion batteries. *Adv. Funct. Mater.* **2025**, *35*, 2423755.

[25] Zhou, J. L.; Ge, T. G.; Cui, X. Z.; Lv, J.; Guo, H. L.; Hua, Z. L.; Shi, J. L. A highly efficient Co_3O_4 nanoparticle-incorporated mesoporous beta composite as a synergistic catalyst for oxygen reduction. *ChemElectroChem* **2017**, *4*, 1279–1286.

[26] Huang, H. J.; Feng, H.; He, Z. Y.; Huang, Y. N.; Xu, J. W.; Hu, C. Z.; Chen, Z. X.; Yang, Z. H.; Zhang, W. X. Enhancing Zn^{2+}/H^+ joint charge storage in MnO_2: Concurrently tailoring Mn's local electron density and O's p-band center. *ACS Nano* **2024**, *18*, 25601–25613.

[27] Zhang, Z. Y.; Zheng, J.; Chen, X. Y.; Yu, X. Y.; Li, L. J.; Bao, L. X.; Peng, J.; Li, X. Achieving ultra-long cycling life for MnO_2 cathode: Modulating Mn^{3+} spin state to suppress Jahn–Teller distortion and manganese dissolution. *Energy Storage Mater.* **2025**, *76*, 104128.

[28] Wang, Y. W.; Zhang, Y. X.; Gao, G.; Fan, Y. W.; Wang, R. X.; Feng, J.; Yang, L. N.; Meng, A. L.; Zhao, J.; Li, Z. J. Effectively modulating oxygen vacancies in flower-like δ-MnO_2 nanostructures for large capacity and high-rate zinc-ion storage. *Nano-Micro Lett.* **2023**, *15*, 219.

[29] Wang, M.; Zhao, G. Y.; Bai, X. M.; Yu, W. J.; Zhao, C. H.; Gao, Z. R.; Lyu, P.; Chen, Z. Y.; Zhang, N. Q. Gradient concentration refilling of N stabilizes oxygen vacancies for enhanced Zn^{2+} storage. *Adv. Energy Mater.* **2023**, *13*, 2301730.

[30] Liu, Y. P.; Wang, H.; Qian, L. X.; Zhao, X. Y.; Yao, L.; Wang, J. Y.; Xing, X. Q.; Mo, G.; Chen, Z. J.; Wu, Z. H. Bismuth-iron-based precursor: Preparation, phase composition, and two methods of thermal treatment. *RSC Adv.* **2020**, *10*, 20713–20723.

[31] Han, X. M.; Zhao, R.; Yu, L. Y.; Wang, L. H.; Zhang, X. Y.; Zhang, A. Q.; Yang, J. J.; Hu, Z. F.; Lv, M. G.; Miao, T. X. et al. Dynamic protective multi-layers for MnO_2 cathodes: Ion sorting and structural protection for superior zinc-ion battery cycling performance. *Adv. Mater.* **2026**, *38*, e13548.

[32] Cao, L.; Chu, M. J.; Li, Y.; Xu, X.; Qiu, Y. W.; Dai, Y.; Sun, C. C.;

Huang, Z. X.; Wu, X. L.; Geng, H. B. *In situ*-constructed multifunctional composite anode with ultralong-life toward advanced lithium-metal batteries. *Adv. Mater.* **2024**, *36*, 2406034.

[33] Qian, S. S.; Xing, C.; Zheng, M. T.; Su, Z.; Chen, H.; Wu, Z. Z.; Lai, C.; Zhang, S. Q. $CuCl_2$-modified lithium metal anode via dynamic protection mechanisms for dendrite-free long-life charging/discharge processes. *Adv. Energy Mater.* **2022**, *12*, 2103480.

[34] Zhang, J. H.; Li, W. B.; Wang, J. J.; Pu, X. H.; Zhang, G. N.; Wang, S.; Wang, N.; Li, X. F. Engineering p-band center of oxygen boosting H^+ intercalation in δ-MnO_2 for aqueous zinc ion batteries. *Angew. Chem., Int. Ed.* **2023**, *62*, e202215654.

[35] Liang, J. R.; Zhao, Y. J.; Ren, L. T.; Li, M. C.; Zhang, Q. L.; Wang, Y. H.; Sun, X. M.; Chuai, M. Y.; Wang, X. S.; Liu, W. Dual anions doping enhanced conductivity and stability of layered *δ*-MnO_2 cathode for aqueous zinc-ion battery. *Adv. Funct. Mater.* **2025**, *35*, 2501135.

[36] Zhao, Y. J.; Zhang, S. X.; Zhang, Y. Y.; Liang, J. R.; Ren, L. T.; Fan, H. J.; Liu, W.; Sun, X. M. Vacancy-rich Al-doped MnO_2 cathodes break the trade-off between kinetics and stability for high-performance aqueous Zn-ion batteries. *Energy Environ. Sci.* **2024**, *17*, 1279–1290.

[37] Zhao, Y. J.; Xia, X. Y.; Li, Q.; Wang, Y. Y.; Fan, Y. C.; Zhao, Y.; Liu, W.; Sun, X. M. Activating the redox chemistry of MnO_2/Mn^{2+} in aqueous Zn batteries based on multi-ions doping regulation. *Energy Stor. Mater.* **2024**, *67*, 103268.

[38] Ye, J.-J.; Li, P.-H.; Hou, Z. G.; Zhang, W.; Zhu, W. H.; Jin, S.; Ji, H. X. Se-dopant modulated selective Co-insertion of H^+ and Zn^{2+} in MnO_2 for high-capacity and durable aqueous Zn-ion batteries. *Angew. Chem., Int. Ed.* **2024**, *63*, e202410900.

[39] Ma, Y.; Xu, M.; Liu, R.; Xiao, H. H.; Liu, Y.; Wang, X.; Huang, Y. Y.; Yuan, G. H. Molecular tailoring of MnO_2 by bismuth doping to achieve aqueous zinc-ion battery with capacitor-level durability. *Energy Stor. Mater.* **2022**, *48*, 212–222.

[40] Wang, H. R.; Guo, R. S.; Ma, Y.; Zhou, F. Cross-doped Mn/Mo oxides with core–shell structures designed by a self-template strategy for durable aqueous zinc-ion batteries. *Adv. Funct. Mater.* **2023**, *33*, 2301351.

[41] Zhang, X.; Ma, X. L.; Bi, H. L.; Zhang, Y. F.; Mi, P. P.; Liu, F. R.; Jin, X. C.; Chen, Y.; Zhang, K.; Wang, J.; et al. Carboxymethylcellulose induced the formation of amorphous MnO_2 nanosheets with abundant oxygen vacancies for fast ion diffusion in aqueous zinc-ion batteries. *Adv. Funct. Mater.* **2024**, *35*, 2411990.

[42] Zheng, W. J.; Cui, Z. B.; Liu, C.; Yuan, L. B.; Li, S. S.; Lin, L. L.; Meng, T.; Yang, L. G.; Tong, Y. X.; Shu, D. Tailoring hierarchical MnO_2 nanostructures on self-supporting cathodes for high-mass-loading zinc-ion batteries. *Chem. Sci.* **2024**, *15*, 20303–20314.

[43] Zhong, W. P.; Zhao, R.; Zhu, Y. R.; Xu, Y. T.; Chen, W. H.; Peng, C. Vacancy engineering on MnSe cathode enables high-rate and stable zinc-ion storage. *Adv. Funct. Mater.* **2024**, *35*, 2419720.

[44] Zhao, X. R.; Zhang, F.; Li, H. Z.; Dong, H. T.; Yan, C. C.; Meng, C.; Sang, Y. H.; Liu, H.; Guo, Y.-G.; Wang, S. H. Dynamic heterostructure design of MnO_2 for high-performance aqueous zinc-ion batteries. *Energy Environ. Sci.* **2024**, *17*, 3629–3640.

[45] Zong, Y.; Chen, H. C.; Wang, J. S.; Wu, M. H.; Chen, Y.; Wang, L. Y.; Huang, X. L.; He, H. W.; Ning, X.; Bai, Z. C. et al. Cation defect-engineered boost fast kinetics of two-dimensional topological bi_2se_3 cathode for high-performance aqueous Zn-ion batteries. *Adv. Mater.* **2023**, *35*, 2306269.

[46] Li, H.; He, Y. Y.; Wang, Q.; Gu, S. N.; Wang, L.; Yu, J. X.; Zhou, G. W.; Xu, L. Q. $SnSe_2/NiSe_2$@N-doped carbon yolk–shell heterostructure construction and selenium vacancies engineering for ultrastable sodium-ion storage. *Adv. Energy Mater.* **2023**, *13*, 2302901.

[47] Yang, M.; Zhu, J. H.; Lai, M. N.; Chen, P. W.; Lin, Y. R.; Li, G. M.; Hu, Q. C.; He, L. J.; Mi, H. W.; Wang, Y. Y. et al. Discovery of D-band center engineered amorphous cathode with ultrahigh, superfast, and wide-temperature Zn^{2+} storage capability. *Adv. Mater.* **2026**, *38*, e20708.

[48] Zhu, Y. R.; Zhao, R.; Xu, Y. T.; Chen, W. H.; Hu, Z. L.; Xi, L. J.; Xie, Y. J.; Hou, H. S.; Liu, T. C.; Amine, K. et al. Anion vacancies coupling with heterostructures enable advanced aerogel cathode for ultrafast aqueous zinc-ion storage. *Adv. Mater.* **2025**, *37*, 2419582.

[49] Yang, M. Q.; Zhu, J. H.; Lin, J.; He, L. J.; Chen, M. F.; Wang, Y. Y.; Chen, J. Z.; Zhong, S. K.; Mi, H. W.; He, C. X. et al. A guest cation screening principle for enabling customized cathode/electrolyte interface chemistry and self-enhanced aqueous zinc-ion batteries. *Angew. Chem., Int. Ed.* **2025**, *64*, e202510893.

[50] Jia, X. X.; Liu, C. F.; Neale, Z. G.; Yang, J. H.; Cao, G. Z. Active materials for aqueous zinc ion batteries: Synthesis, crystal structure, morphology, and electrochemistry. *Chem. Rev.* **2020**, *120*, 7795–7866.

[51] Wan, F.; Zhou, X. Z.; Lu, Y.; Niu, Z. Q.; Chen, J. Energy storage chemistry in aqueous zinc metal batteries. *ACS Energy Lett.* **2020**, *5*, 3569–3590.

[52] Cui, S. S.; Zhang, D.; Gan, Y. Traditional electrochemical Zn^{2+} intercalation/extraction mechanism revisited: Unveiling ion-exchange mediated irreversible Zn^{2+} intercalation for the δ-MnO_2 cathode in aqueous Zn ion batteries. *Adv. Energy Mater.* **2024**, *14*, 2302655.

This is an open access article under the terms of the Creative Commons Attribution 4.0 International License (CC BY 4.0, https://creativecommons.org/licenses/by/4.0/).

© The Author(s) 2026. Published by Tsinghua University Press.